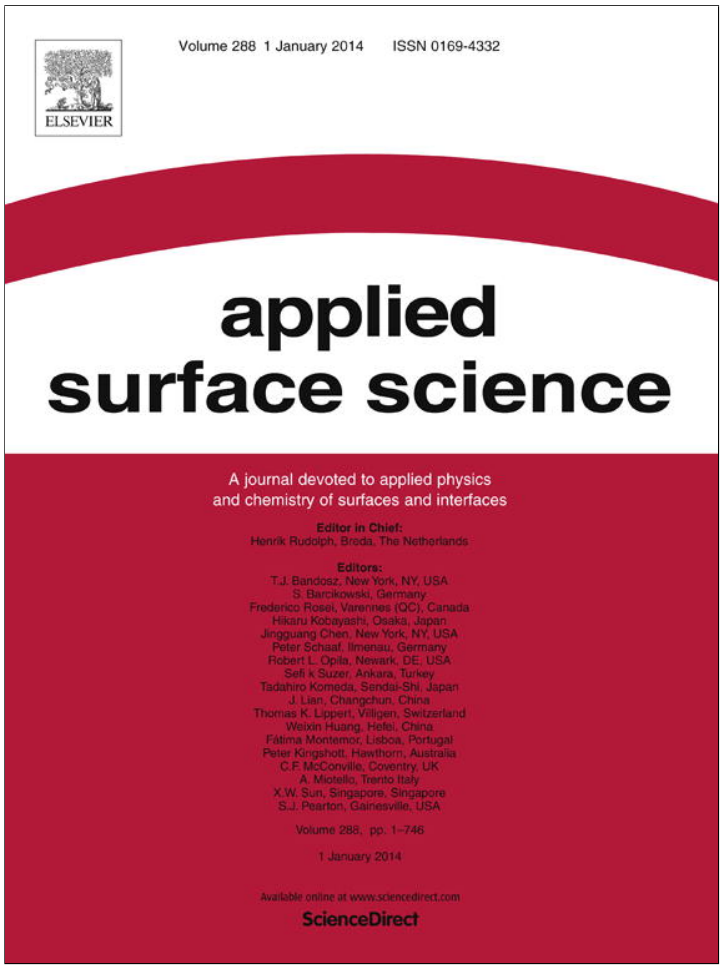

Applied Surface Science 288 (2014) 313–323

Contents lists available at ScienceDirect

Applied Surface Science

journal homepage: www.elsevier.com/locate/apsusc

Surface morphology and phase transformations of femtosecond laser-processed sapphire

R. Vilar[a,b], S.P. Sharma[a,b], A. Almeida[a,b,*], L.T. Cangueiro[a,b], V. Oliveira[a,c]

[a] Instituto de Ciência e Engenharia de Materiais e Superfícies (ICEMS), Instituto Superior Técnico, Av. Rovisco Pais, 1049-001 Lisboa, Portugal
[b] Instituto Superior Técnico, Universidade de Lisboa, Av. Rovisco Pais, 1049-001 Lisboa, Portugal
[c] Instituto Superior de Engenharia de Lisboa, Avenida Conselheiro Emídio Navarro No. 1, 1959-007 Lisboa, Portugal

ARTICLE INFO

Article history:
Received 9 July 2013
Received in revised form 1 October 2013
Accepted 4 October 2013
Available online 12 October 2013

Keywords:
Sapphire
Femtosecond laser ablation
Self-ordered periodic structures
Ablation debris

ABSTRACT

The morphological and structural modifications induced in sapphire by surface treatment with femtosecond laser radiation were studied. Single-crystal sapphire wafers cut parallel to the (0 1 2) planes were treated with 560 fs, 1030 nm wavelength laser radiation using wide ranges of pulse energy and repetition rate. Self-ordered periodic structures with an average spatial periodicity of ~300 nm were observed for fluences slightly higher than the ablation threshold. For higher fluences the interaction was more disruptive and extensive fracture, exfoliation, and ejection of ablation debris occurred. Four types of particles were found in the ablation debris: (a) spherical nanoparticles about 50 nm in diameter; (b) composite particles between 150 and 400 nm in size; (c) rounded resolidified particles about 100–500 nm in size; and (d) angular particles presenting a lamellar structure and deformation twins. The study of those particles by selected area electron diffraction showed that the spherical nanoparticles and the composite particles are amorphous, while the resolidified droplets and the angular particles, present a crystalline α-alumina structure, the same of the original material. Taking into consideration the existing ablation theories, it is proposed that the spherical nanoparticles are directly emitted from the surface in the ablation plume, while resolidified droplets are emitted as a result of the ablation process, in the liquid phase, in the low intensity regime, and by exfoliation, in the high intensity regime. Nanoparticle clusters are formed by nanoparticle coalescence in the cooling ablation plume.

1. Introduction

The interactions between nanosecond laser pulses and materials are essentially thermal in nature. On the contrary, due to their extremely high peak intensity and short pulse duration, high radiation intensity femtosecond lasers minimize the contribution of thermal phenomena to the ablation process [1]. In fact, due to their ultrahigh intensity, these lasers induce non-linear electron excitation processes such as multiphoton ionization, which promote electrons to the conduction band despite the photon energy being lower than the energy gap. The increase of the electron density in the conduction band leads to an increase of the radiation absorption coefficient and of the reflectivity. On the other hand, electrons in the conduction band absorb very effectively the laser radiation by inverse bremsstrahlung and ionize other atoms by collisional excitation, eventually leading to an avalanche and the formation of a plasma [1]. It is generally assumed that, when the electron density reaches the critical plasma density, i.e. the electron density where the plasma frequency equals the frequency of the laser, ablation occurs [1,2]. Due to the very high values of the radiation absorption coefficient in the plasma the radiation/material energy transfer process is localized within an extremely shallow surface layer and energy absorption by the surrounding material is negligible. For low radiation intensities, in general corresponding to longer laser pulses for similar pulse energy, there is still a large thermal contribution. Energy is transferred from the excited electrons to the lattice within a few picoseconds after the end of the laser pulse, leading to material melting, bubble nucleation and material ejection [1]. For higher values of intensity (larger than about 10^{13} W/cm^2) ablation is essentially athermal [3]. This ablation mechanism, designated by electrostatic ablation, involves photoemission of electrons from the surface followed by electrostatic ejection of the remaining positively charged particles [1,3,4]. Since the excitation process is highly non-linear, the laser effects can be extremely localized and confined to a small focal volume. This localization is further enhanced by the fact that heat transport during the ultra-short laser pulse duration is negligible.

Lasers allow writing periodic or aperiodic surface textures in many materials. Aperiodic micron-sized textures characterized by

* Corresponding author at: Instituto Superior Técnico, Universidade de Lisboa, Av. Rovisco Pais, 1049-001 Lisboa, Portugal. Tel.: +351 218419176.
E-mail address: amelia.almeida@ist.utl.pt (A. Almeida).

0169-4332/$ – see front matter © 2013 Elsevier B.V. All rights reserved.
http://dx.doi.org/10.1016/j.apsusc.2013.10.026

features such as columns, cones, etc. have been studied since many years in surfaces treated with nanosecond pulse duration lasers at fluences slightly higher than the ablation threshold. Their formation mechanisms were the object of intense discussion during more than one decade, radiation shadowing by impurities [5], differential ablation [6,7], hydrodynamic effects [8] or inhomogeneity of the material structure [9] being some of the suggested causes leading to their formation. Surface relief can also appear in thin films deposited by LCVD [10]. When surfaces are submitted to short duration laser pulses parallel ripples with periods in the range 200–800 nm and amplitude 10–100 nm, known as Laser-Induced Periodic Surface Structures (LIPSS), form in a wide range of materials, including semiconductors, metals and dielectrics [11,12]. Their formation was explained by the interference of the incident electromagnetic wave with surface Plasmon polaritons, i.e. electromagnetic modes bound to and propagating along the surface, created by the incident wave coupling with scratches, dust particles and other surface defects [13–15]. A consequence of this mechanism is that LIPSS are perpendicular to the laser beam polarization vector. LIPSS affect important surface properties, such as wetting [16–19], biocompatibility [20], cell adhesion and proliferation behavior [21] and several optical properties [22], and are being actively investigated since several years. A different type of periodic self-organized structures are the parallel nanogratings formed by tightly focusing femtosecond duration laser pulses inside materials such as silica [23,24] or sapphire [25,26]. These nanogratings are perpendicular to the radiation polarization vector as well [27]. Their formation was explained by an inhomogeneity of the plasma distribution within the focal volume created when the incident laser beam interacts with plasmons at the dielectric-plasma interface, leading to periodic field enhancement and further ionization in these periodic nanoplanes. Other types of effects are also observed. When the laser beam is focused within a transparent material, such as silica or sapphire, with intensities near or exceeding 10^{13} W/cm^2, voids typically ~250 nm in diameter are created [28]. These voids are surrounded by a layer of a phase denser than the original material, because the total volume remains constant. Gamaly et al. [29] studied the mechanism of formation of these voids and concluded that the material within the volume affected by the laser radiation (similar to the focal volume ~0.15 μm^3) is ionized and converted into superhot expanding plasma, leading to extremely high temperatures and pressures. Using modeling Glezer and Mazur [28] estimated that if only 30% of the energy of the plasma created by the laser beam is transferred to the surrounding material, the temperature will reach ~10^6 K and the pressure about 3000 GPa. The expansion of this confined plasma leads to the formation of a spherical shockwave that propagates from the focal volume into the material, compressing it. On the other hand, a rarefaction wave propagates to the center originating the void [30–33]. The compression wave may induce the transformation of crystalline sapphire into the amorphous phase, which is 1.14 times denser than the crystalline form. In agreement with the predictions, Juodzakis et al. [32,34] found that a tear-shaped nanovoid surrounded by a shell of amorphous material was created within sapphire for laser beam intensities higher than 10^{14} W/cm^2 as a result of the extremely high temperatures and pressures generated by the focal volume, which the authors estimated at 5×10^5 K and 10 TPa. A value of about 10^{18} K/s was estimated for the cooling rate. For lower intensities no void is formed and a tear shape region of amorphous alumina forms [33]. This amorphous alumina is etched by a HF solution or by the ion milling operation used to prepare transmission electron microscopy thin foils so it appears as nanovoid after etching [34]. The amorphous alumina will crystallize upon irradiation with multiple laser pulses leading to the formation of nanocrystalline material [33]. Nanocracks preferentially oriented along the basal plane of sapphire were observed [31].

The aim of this paper is to study surface topography and phase transformations induced by the ablation of single crystalline sapphire. Sapphire or α-alumina is a crystalline material widely used in the optoelectronic industry. It is brittle and extremely hard and, consequently, difficult to machine using conventional methods, so machining with ultrafast lasers is an interesting alternative to conventional machining processes for the manufacturing of parts such as lenses, high-pressure windows, displays, cutting blades, surgical tips, biomedical equipment, sensors, etc. [35]. However, up to this moment very few studies exist on ultrafast laser processing of sapphire.

2. Experimental methods

2.1. Material processing

The specimens were 10 mm × 5 mm × 1 mm sapphire single crystalline wafers with both faces polished supplied by *CrysTec GmbH, Berlin*. The laser treatments were performed in air using an Yb:KYW chirped-pulse-regenerative amplification laser system (Amplitude Systèmes sPulse HP, Bordeaux) with a radiation wavelength of 1030 nm and a pulse duration of 560 fs. The laser beam was focused perpendicularly to the specimen surface by a 40× high numerical aperture (0.66) microscope objective. The experiments were carried out with stationary sample and laser beam or by translating the sample with respect to the stationary laser beam at constant scanning speed using a computer controlled linear stage. In order to investigate the influence of the processing parameters on the surface topography and material structure, the pulse energy and pulse repetition rate were varied within the ranges 4–100 μJ and 1–100 kHz, respectively. The scanning speed was varied from 0.01 to 2.0 mm/s.

The ablation threshold was calculated on the basis of measurements of the diameter of craters produced with 10, 20 and 40 laser pulses at a repetition rate of 1 Hz and with fluences between 12.5 and 125 J/cm^2. The measurements were carried out on calibrated SEM images using ImageJ software [36]. To compensate for the asymmetry of the craters four diameters were measured in different directions for each crater and an average calculated. Five craters were measured for each set of laser processing parameters. The ablation threshold was calculated using the D^2-method described by Liu [37]. The basis of the method is as follows. Assuming a Gaussian laser beam the maximum fluence (ϕ_0) and the laser pulse energy (E_p) can be related by:

$$\phi_0 = \frac{2E_p}{\pi w_0^2} \tag{1}$$

where w_0 is the laser beam radius at e^{-2} of the maximum intensity. On the other hand, the diameter of an ablation crater (D) is related with the maximum fluence (ϕ_0) by

$$D^2 = 2\,w_0^2\,\ln\left(\frac{\phi_0}{\phi_{th}}\right) \tag{2}$$

where ϕ_{th} is the ablation threshold fluence. As a result, the Gaussian beam radius w_0 can be calculated from a plot of the square of the average crater diameter vs. the logarithm of the pulse energy. The peak fluence can then be calculated from the pulse energy and the laser beam radius at e^{-2}. Knowing this value, the ablation threshold for a given number of laser pulses can be determined by extrapolating to zero a linear plot of the square of the crater diameter (D) as a function of the logarithm of the fluence.

2.2. Specimens characterization

The processed surfaces were observed by scanning electron microscopy using a JEOL JSM-7001F field emission gun scanning

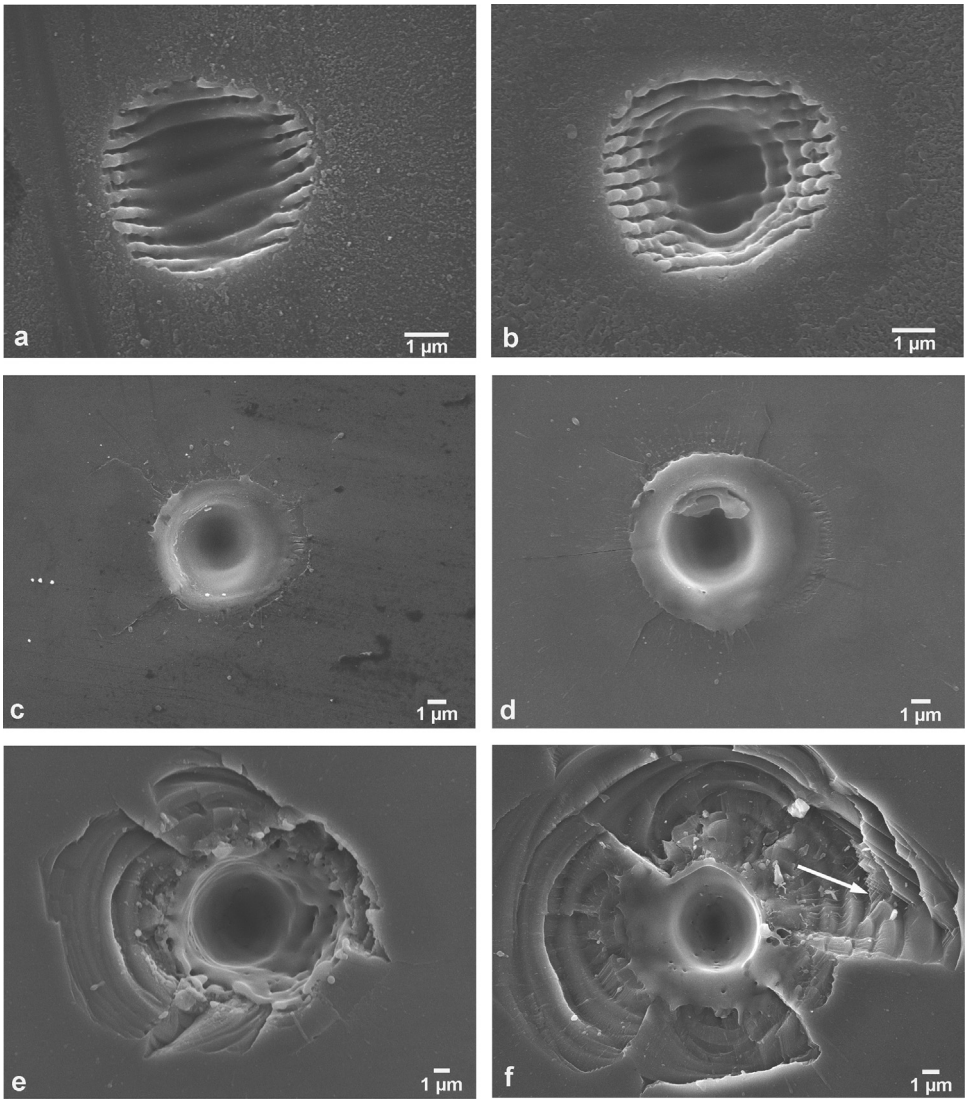

Fig. 1. Craters created in sapphire with a stationary laser beam at a frequency of 1 kHz. (a) 10 μJ, 20 pulses; (b) 10 μJ, 40 pulses; (c) 20 μJ, 10 pulses; (d) 30 μJ, 20 pulses; (e) 30 μJ, 40 pulses; (f) 50 μJ, 40 pulses.

electron microscope (FEG-SEM), operated at 15 kV. Due to the insulating character of sapphire the specimens were gold coated before scanning electron microscopy observations using a Polaron E-5100 sputter coater to prevent charge accumulation.

The phase constitution was investigated by X-ray diffraction (XRD) and micro Raman spectroscopy. XRD was performed with a Panalytical X'Pert diffractometer using CuKα radiation. The scanning range was 20°–80°, the step size 0.01° and the integration time 5 s. MicroRaman spectroscopy was carried out using a Horiba LabRAM HR800 Evolution (Jobin-Yvon, France) spectrometer. The radiation source was a solid-state laser operating at 532 nm with an output power of 12 mW. A spectrograph with an 1800 lines/mm grating was used to provide a spectral resolution of 0.5 cm^{-1}, and the confocal hole size was set at 200 μm. A 100× objective lens focused the laser beam to a 0.72 μm spot on the samples' surface. The spectra were obtained with an acquisition time of 30 s and 3 accumulations. Before the measurements the system was calibrated to better than 1 cm^{-1} using a silicon sample. The spectra were normalized to the most intense band, at ca. 418 cm^{-1}.

The ablated particles were characterized by transmission electron microscopy using a Hitachi H-8100 microscope equipped with a Thermo Noran System Six energy dispersive spectroscopy attachment for chemical microanalysis. The particles were extracted by immersing the samples in a small volume of ethanol and ultrasonicating for 15 min to disperse the ablation debris. A few drops of the suspension were poured onto 300 mesh Cu grids with carbon support film and the liquid dried at room temperature.

Standardless EDS analyses and selected area electron diffraction (SAED) and microdiffraction experiments were performed with a 15 nm nominal probe diameter. Experimental electron diffraction patterns were compared with patterns simulated using CaRIne Crystallography© simulation software.

3. Results

3.1. Ablation threshold

Craters created in sapphire with a stationary laser beam at a frequency of 1 kHz and pulse energies between 10 and 50 μJ are shown in Fig. 1a–f. The craters present scarce evidence of melting and are surrounded by re-deposited debris. The crater produced with 20 laser pulses at 10 μJ (2.5×10^{13} W/cm^2) (Fig. 1a) presents a hemispherical shape and is covered by parallel ripples (LIPSS). The average LIPSS spacing is 300 ± 15 nm. Increasing the number of pulses to 40 (Fig. 1b) increases the crater depth but an embedded

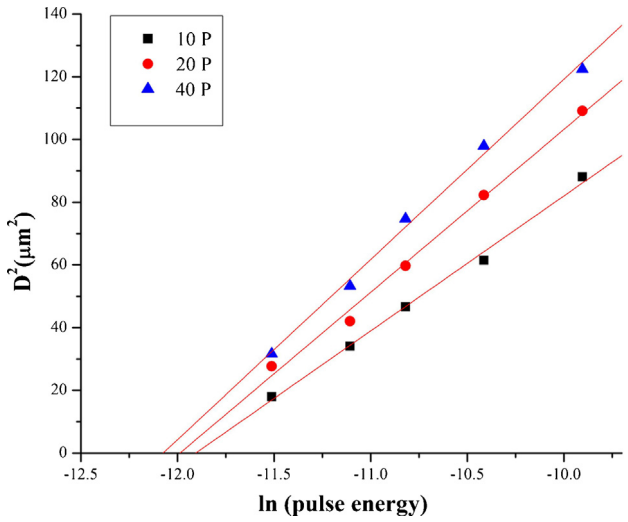

Fig. 2. Semi-logarithmic plots of the square of the crater diameter (D^2) in function of the pulse energy for 10, 20 and 40 laser pulses.

nanostructure is still observed. On the contrary, the ripples disappear for higher intensities (Fig. 1c–f). The crater produced at 10 laser pulses and 20 μJ, corresponding to an intensity of 5×10^{13} W/cm^2 (Fig. 1c), presents a well-defined hemispherical shape and is free of cracks and ripples, but for larger intensities and number of pulses (Fig. 1d–f) cracking occurs, eventually leading to extensive exfoliation for 40 laser pulses both at 30 μJ (Fig. 1e) and 50 μJ (Fig. 1f). The fractured craters present steps approximately parallel to the surface of the sample (Fig. 1e and f) and, in some regions, a faceted morphology (indicated by the arrow in Fig. 1f). Contrarily to the precedent samples, angular debris appear in and around these craters, produced by thermo-mechanical stress-induced exfoliation (Fig. 1e and f). The shape of the craters varies with the radiation intensity, becoming increasingly flat at the bottom for increasing values of the intensity.

Fig. 2 presents semi-logarithmic plots of D^2 in function of the pulse energy for 10, 20 and 40 laser pulses. Application of the extrapolation method previously described leads to values of the ablation threshold of 15.6 ± 1.8, 14.3 ± 1.5 and 12.2 ± 1.0 J/cm^2 for 10, 20 and 40 pulses, respectively.

3.2. Morphology of laser tracks

The morphology of tracks produced by scanning the laser beam focused at the specimen surface, with a pulse repetition rate of 1 kHz, are shown in Fig. 3. The pulse energies were 10, 25, 50 and 100 μJ, corresponding to fluences of 12.5, 31.3, 62.6 and 125 J/cm^2, respectively. The variation of the tracks width and depth with the pulse energy is plotted in the graph of Fig. 4. The width and depth of the tracks increase with increasing pulse energy. The track morphology depends significantly on the pulse energy. For the lowest pulse energy (10 μJ), LIPSS form at the bottom of the track. For higher pulse energies LIPSS form only at the periphery of the tracks, in the region of lower fluence, reflecting the Gaussian intensity distribution in the laser beam, and for the higher values of fluence no LIPSS are observed.

Self-ordered periodic structures formed at the surface of the specimen with a linearly polarized laser beam are oriented perpendicularly to the polarization vector. The structures obtained with the polarization vector aligned with the scanning direction, pulse

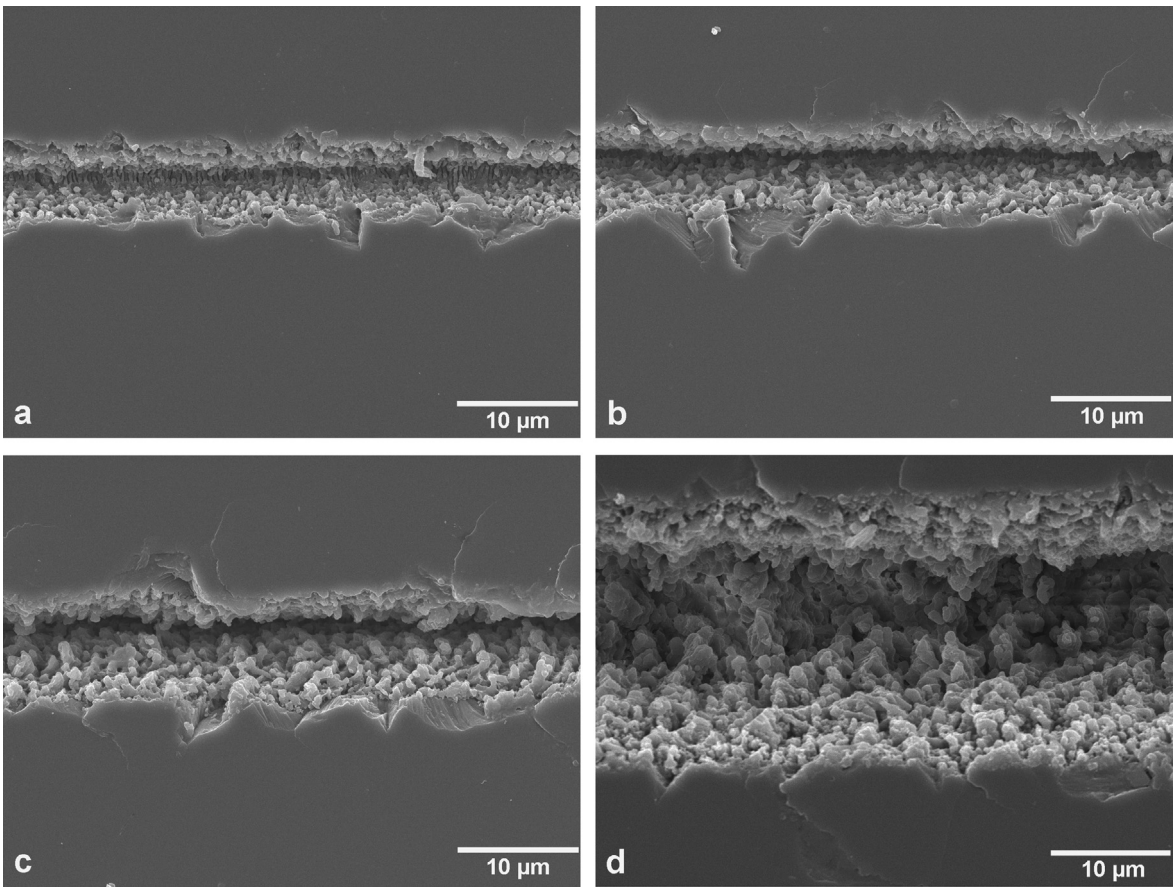

Fig. 3. Morphology of laser surface tracks produced with a pulse repetition rate of 1 kHz and different pulse energies: (a) 10 μJ; (b) 25 μJ; (c) 50 μJ; (d) 100 μJ.

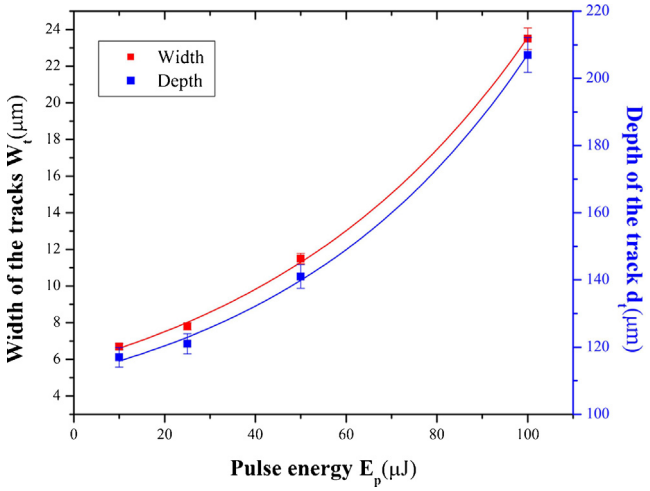

Fig. 4. Variation of the width and depth of tracks produced with a pulse repetition rate of 1 kHz and different pulse energies with respect to pulse energy.

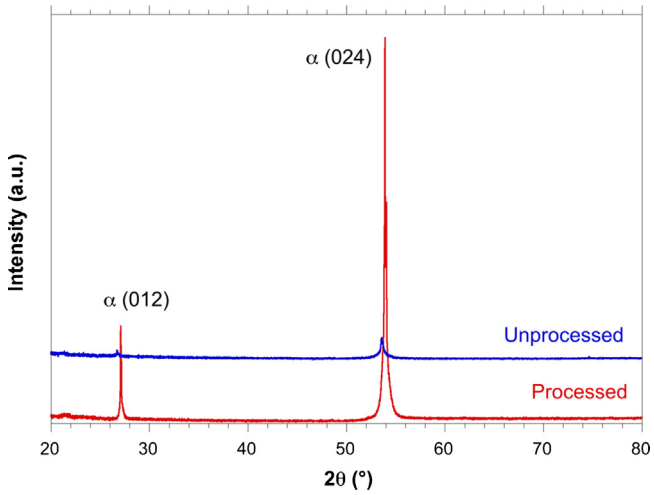

Fig. 6. X-ray diffractograms of specimens in the pristine condition and after laser processing with a pulse energy of 4 μJ and a pulse repetition rate of 100 kHz.

energy 4 μJ and pulse repetition rates of 1 and 100 kHz are shown in Fig. 5a and b, respectively. Their average periodicity is 284 nm and 315 nm. In general, the period of these structures varies between 250 and 350 nm within the parameters ranges used.

The chemical composition of the material is modified by laser processing. The O/Al ratios measured by EDS at the areas indicated by 1, 2 and 3 in Fig. 5b at the center, edge and outside the track are 1, 1.5 and 1.5. Despite the low accuracy in the determination of oxygen by EDS and the effect of topography, a significant difference between the values of this ratio in processed and unprocessed regions was systematically observed, the concentration of oxygen in the laser processed material being always lower than the value for stoichiometric alumina.

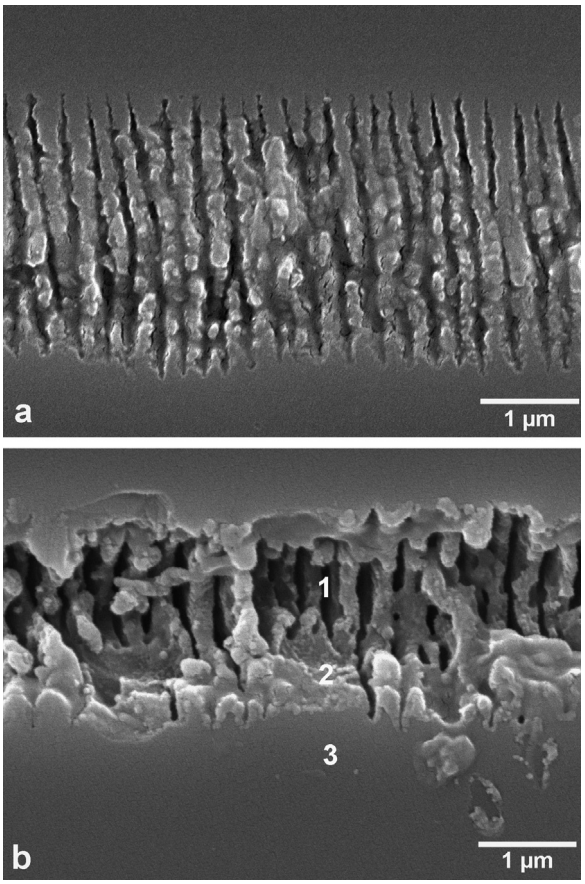

Fig. 5. Self-ordered periodic structures produced at the specimen surface with pulse energy of 4 μJ and pulse repetition rates of (a) 1 kHz and (b) 100 kHz. 1, 2 and 3 indicate regions where EDX spectra were acquired.

3.3. X-ray diffraction analysis

Fig. 6 shows typical X-ray diffractograms of an unmodified specimen and a specimen where a large number of parallel laser surface tracks were produced at 4 μJ and a pulse repetition rate of 100 kHz. Both diffractograms consist only of two peaks that can be indexed as (0 1 2) and (0 2 4) peaks of sapphire, confirming that the crystal was cut parallel to the (0 1 2) plane. Laser processing causes a reduction of the interplanar distances of the (0 1 2) and (0 2 4) planes from 0.3339 to 0.3302 nm and 0.1710 to 0.1701 nm, respectively, an effect that is probably due to the residual stresses induced by the laser treatment.

3.4. Micro Raman analysis

The absence of phase transformations due to the laser treatment was also confirmed by Raman spectroscopy. Raman spectra of specimens in the pristine condition and after laser processing with 20 μJ energy and 1 kHz pulse repetition rate are shown in Fig. 7. Both spectra present seven bands situated at 379, 417.5, 430.5, 448.5, 476.6, 644 and 750 cm^{-1}, typical of sapphire [38]. Both the XRD and the Raman spectroscopy results show that laser processing does not induce significant changes in the phase constitution of α-alumina.

3.5. Morphology and crystallographic structure of the ablation debris

Different types of particles were observed in the ablation debris (Fig. 8a–d). The particles shown in Fig. 8a present a spherical shape and an average diameter of 50 ± 4 nm. They often form clusters, but the forces that held these clusters together are weak (van der Waals and/or capillary forces) and they are easily dispersed under the electron beam during observation. The cluster shown in Fig. 8b includes particles of this type but it is mainly formed of resolidified droplets with typical sizes in the range 100–500 nm and spherical to elliptical shape. Fig. 8c illustrates a particle formed of a number of nanoparticles similar to those presented in Fig. 8a, which fused together, forming necks between them. Finally, in Fig. 8d a particle

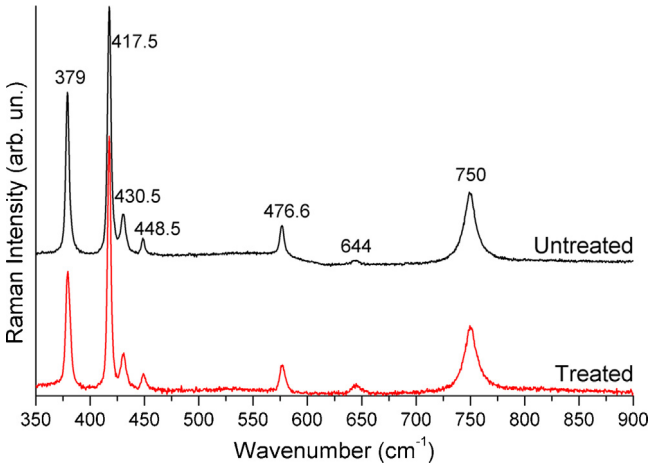

Fig. 7. Raman spectra of specimens in the pristine condition and after laser processing with a pulse energy of 20 μJ and a pulse repetition rate of 1 kHz.

with angular shape, lamellar morphology, and presenting a large number of twins is shown. The presence of twins indicates that this particle was submitted to intense stresses and deformation.

The crystallographic structure of a number of particles of each type was studied by selected area electron diffraction (SAED). Fig. 9a and b depict a bright field TEM image and a SAED pattern of a cluster of spherical nanoparticles similar to those shown in Fig. 8a. The diffraction pattern does not present any diffraction spots or rings and is characteristic of an amorphous material. A similar SAED pattern was obtained for particles resulting from coalescence of these nanoparticles (Fig. 9c) On the contrary, the SAED pattern of cluster containing resolidified droplets presents diffraction spots distributed in distinct rings, which can be indexed as α-alumina phase, as well as a diffuse central spot typical of an amorphous phase. Taking into consideration the previously presented results, it is clear that the smaller particles in the bimodal particle size clusters are amorphous while the larger particles are crystalline (Fig. 9e).

Fig. 10 presents the SAED analysis of a particle with irregular shape and layered structure, similar to the one depicted in Fig. 8d. For each electron diffraction pattern, the simulated pattern for the corresponding zone axis is also presented. The diffraction patterns may be indexed to the crystalline α-Al_2O_3 phase.

4. Discussion

The ablation threshold of dielectric materials increases approximately linearly with the material band-gap energy [39]. Pure sapphire presents a band gap of 8.8 eV, but the ablation behavior depends on the material structure, surface finish and experimental conditions. The ablation threshold of the single crystalline sapphire wafers with surface parallel to the (0 1 2) planes used in the present work was 15.6 ± 1.8, 14.3 ± 1.5 and 12.2 ± 1.0 J/cm^2 for 10, 20 and 40 laser pulses, respectively. These values are higher than those found by Henyk et al. [40] (2.2 J/cm^2 for five hundred 120 fs laser pulses @800 nm), Li et al. [41] (4.5 J/cm^2 for five 45 fs laser pulses @800 nm), Watanabe et al. [39] (4.2 J/cm^2 for one 180 fs laser pulse @800 nm) and Christensen et al. [42] (8 ± 2 J/cm^2 for one 100 fs laser pulse @800 nm). This discrepancy can be explained by the fact that the ablation threshold in the femtosecond and picosecond pulse duration regimes increases with increasing pulse duration [42,43] and with decreasing beam spot radius [43], and the pulse duration

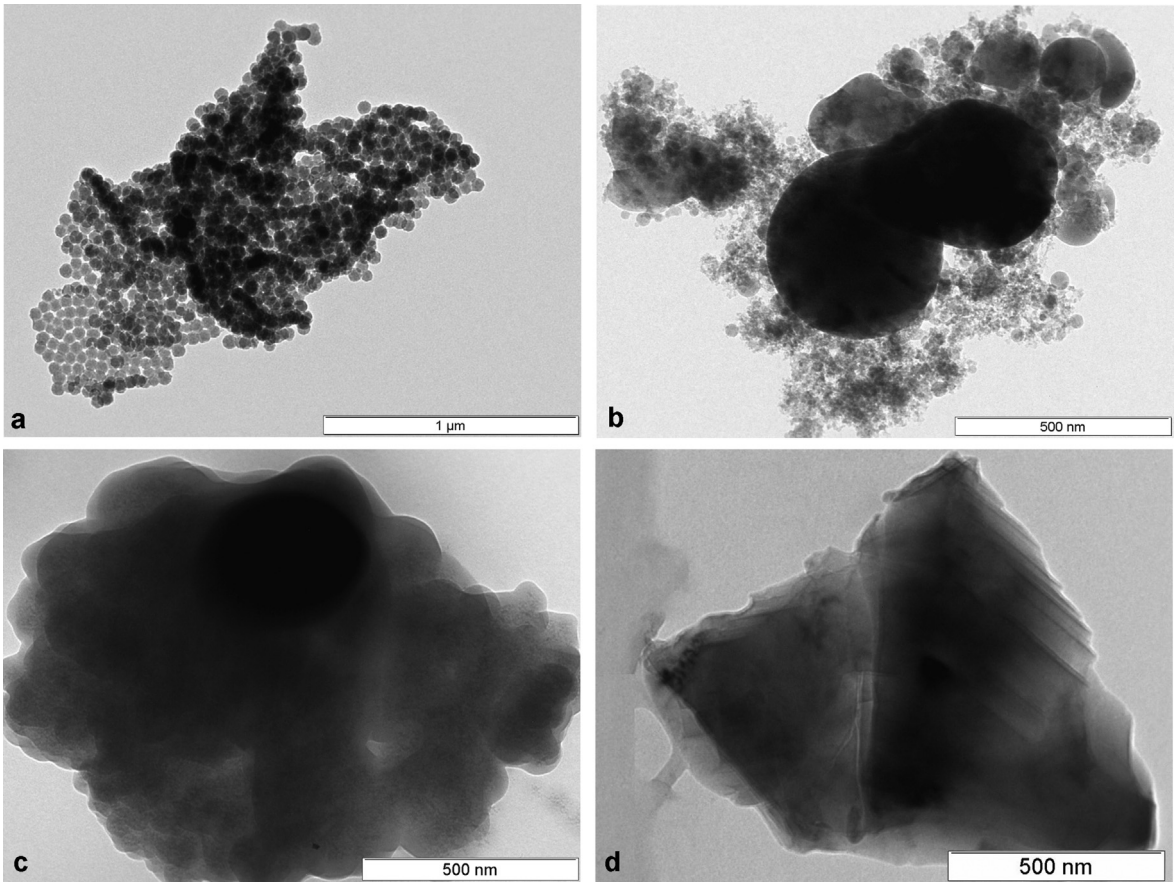

Fig. 8. Morphology of the particles observed in the ablation debris.

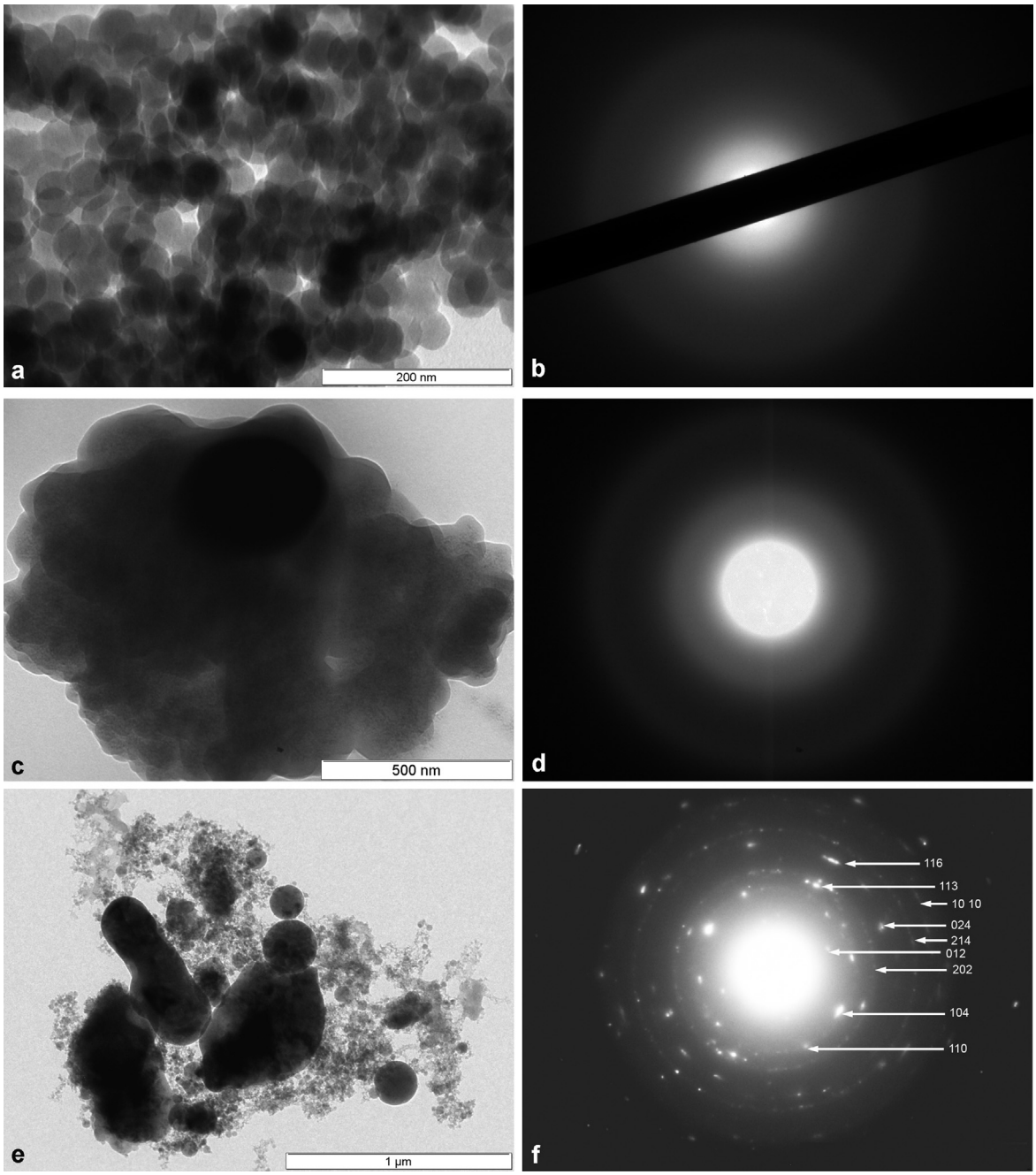

Fig. 9. TEM images and SAED patterns of particles produced in ablation experiments carried out with a pulse energy of 10 μJ, pulse repetition rate of 1 kHz and scanning speed of 0.1 mm/s.

used in the present work is larger than that used by the precedent authors. In agreement with this interpretation, Uteza et al. [43] measured thresholds of 18.5 and 210 J/cm^2 for 50 ps and 8 ns pulse durations, consistent with the values found in the present work. The decrease of the ablation threshold with increasing number of laser pulses, observed in the present paper, is in agreement with the results of Watanabe et al. [39] and can be explained by the formation of color centers during the first laser pulses, which increase the material absorption coefficient and facilitate the generation of free carriers during subsequent laser pulses. The evolution of the crater shape from semispherical to flat bottom with increasing radiation intensity, visible in Fig. 1, was explained theoretically by Jiang and Tsai [2]. Ionization of the dielectric material by intense laser radiation leads to an increase of the electron density in the conduction band. For ablation to occur the electron density must exceed the critical electron density and for these electron densities the dielectric body behaves pretty much as a metal, with extremely high reflectivity. Due to the Gaussian shape of the beam ionization and, consequently, reflectivity is larger at the center of the irradiated area, reducing the ablation rate in this region and flattening the crater bottom.

The nanostructures observed in Fig. 1 are similar to those observed in the same material by Juodkakis et al. [31], Wortmann et al. [25], Kim et al. [44], and Bai et al. [26]. They differ from the nanogratings that form within dielectric materials when they are irradiated by tightly focused femtosecond laser beams [23,27] and can be considered LIPSS. The formation of these surface ripples was explained by Keilmann and Bai [13] and Sipe et al. [14]. They

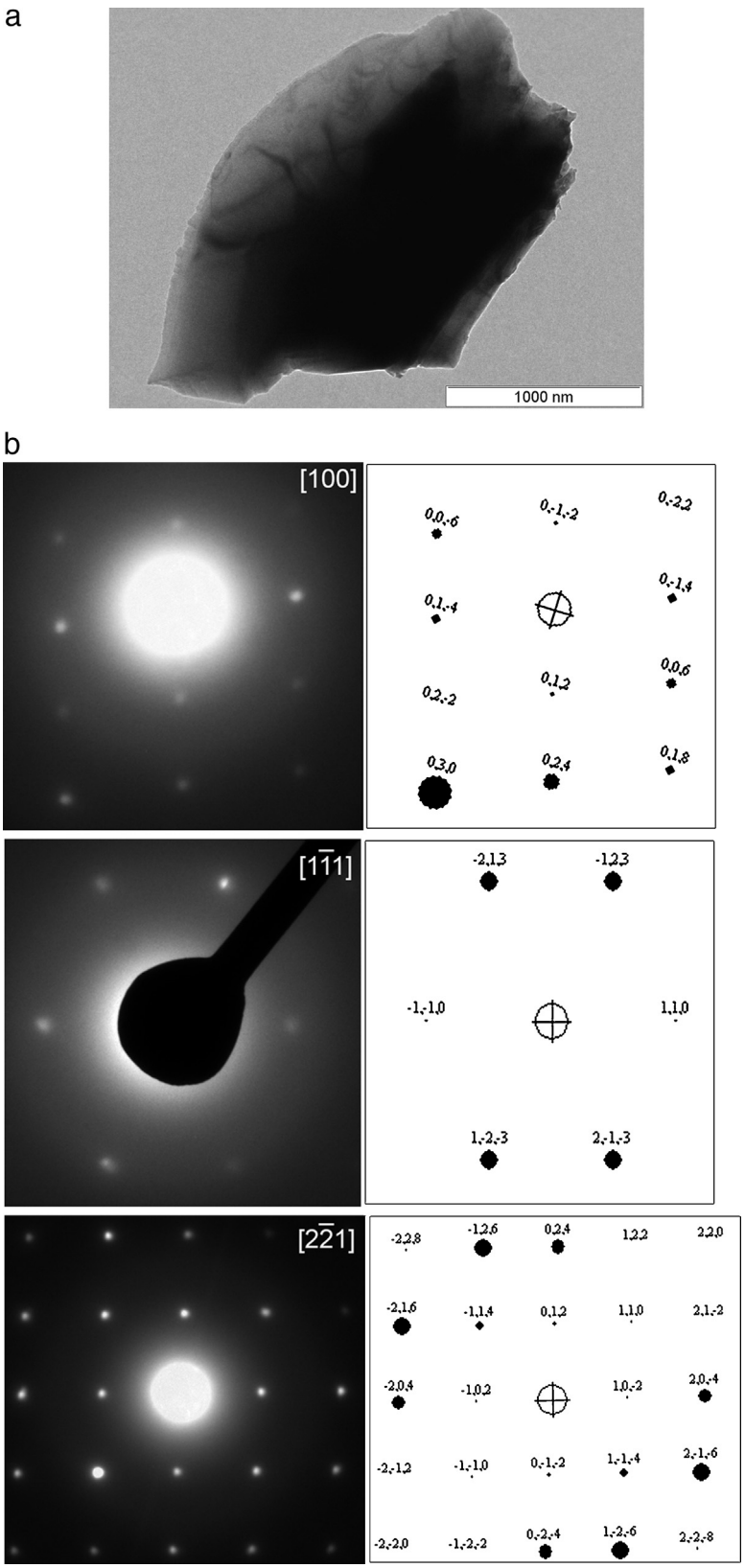

Fig. 10. (a) TEM image and (b) SAED patterns and respective simulated patterns of a particle produced with a pulse energy of 25 μJ, pulse repetition rate of 1 kHz and scanning speed of 0.1 mm/s.

result from an inhomogeneity of the radiation energy absorbed just beneath the surface due to the interference of the incident beam with surface plasmonic waves originated by the scattering of the incident wave by surface defects. Consistent with this model and observations of previous authors, the gratings are parallel to the beam polarization vector. Their period (300 nm) is similar to the periods of the ripples observed by Juodkakis et al. [31] (267 nm @800 nm) and slightly larger than that of Kim et al. [44]

(239–255 nm @800 nm), but the results are consistent with these because the period of LIPSS increases with increasing scanning speed [44] and the scanning speeds used in the present experiments are larger than those used by these authors.

Laser processing with high pulse energies leads to the fracture of sapphire and extensive exfoliation to the point that thus becomes the predominant ablation mechanism of sapphire in these regimes. Alumina is a hard, brittle material with a hexagonal-rhombohedral structure. Fracture in sapphire usually nucleates at microcracks in the regions of maximum tensile stresses and advances as a mode I crack, obeying the Griffith's energy balance criterion [45]. According to this criterion, fracture in an opening mode occurs at the point and in the direction of the maximum tensile stress σ_0, when it reaches the critical value (σ_0^c) of

$$\sigma_0^c = \left(\frac{EG_c}{\pi a}\right)^{1/2} \quad (3)$$

where a is the length of the pre-existing crack, $G_c = 2\gamma$ is the energy available for crack growth, γ the energy required to form a unit of new material surface and E is the Young's modulus [46]. Sapphire has 3 low energy cleavage plane families $\{1\,0\,\bar{1}\,0\}$, $\{1\,1\,\bar{2}\,0\}$ and $\{1\,0\,\bar{1}\,2\}$, so cracks propagate along one of these planes or, if this is not possible, a combination of two or more intersecting planes. This explains the stepped morphology observed in the craters of Fig. 1e and f.

The O/Al atomic ratio in non-ablated areas is 1.5, in agreement with the stoichiometric Al_2O_3 value, but lower values of this ratio were observed in the ablated regions. This variation of chemical composition can be explained by the laser-induced emission of positive O^+ ion, as well as molecular fragments containing oxygen in the ablation of sapphire [40]. To the best of our knowledge, no systematic study of the composition changes due to ultrafast laser ablation of alumina was carried out so far, but Lancry et al. [47] suggested that the nanostructures formed within amorphous silica by femtosecond laser irradiation result from the decomposition of silica in the regions of higher radiation intensity and are accompanied by gaseous oxygen release. A decrease of the oxygen content was also observed in nanoplanar structures formed in alumina by femtosecond laser treatment [44].

The mechanisms of formation of particles by ultrafast laser ablation were reviewed by Semaltianos et al. [48]. Nanoparticles may be ejected as a result of the ablation process or form during the cooling down of the ablation plume. Molecular dynamics simulations carried out by Perez and Lewis [49] showed that, for sufficiently high pulse energies, nanoparticles are emitted directly from the target by a photomechanical process that the authors called fragmentation whereby the initially homogeneous superheated liquid relaxes transforming into clusters. The cluster size can be estimated on the basis of Ashurt and Holian [50] model assuming that the strain energy accumulated in the fluid is converted into surface energy. On the other hand, the interaction of the laser beam with the material leads to the formation of a plume consisting mainly of neutrals and ionized species. The plume expands adiabatically, compressing the background gas. At the maximum of its expansion an inversion of the pressure gradient occurs and the plume contracts while cooling down, resulting in the formation of nanoparticles by a nucleation and growth mechanism. Noel et al. [51] and Itina et al. [52] detected two populations of nanoparticles in femtosecond laser ablation plumes, one, with average particle size smaller than 7 nm, consists of clusters directly emitted during ablation, and the other, with larger diameter particles, which consists of particles formed by condensation in the plume. These two types of particles are present in the ablation debris collected in the present work. The characteristics of spherical nanoparticles observed in Fig. 8a are consistent with the direct nanoparticle emission mechanism proposed by Perez and Lewis [49]. They present an amorphous structure as a result of the extremely high cooling rates observed in the plume as it contracts. The particles represented in Fig. 8c consist of several nanoparticles fused together into a larger particle and present an amorphous structure as well. It is suggested that they form by aggregation and sintering of nanoparticles during the plume cooling down. The larger particles shown in Fig. 8c may result from the evolution of particles of the precedent type accompanied by crystallization of the material. They may also be ejected in the liquid phase and crystallize during cooling to room temperature. The process leading to the formation of angular particles such as those observed in Fig. 8d is certainly laser-induced thermo mechanical fracture and exfoliation [53]. These angular particles present clear evidence of deformation and fracture. The most frequently observed deformation modes in α-alumina are basal slip and basal twinning. Sapphire being a brittle material deformation is usually accompanied by cracking. Microcracks can nucleate either at basal twin interfaces or from pyramidal slip planes [54]. Staehler et al. [55] showed that the uniaxial compressive fracture strength of sapphire was strongly dependent on the strain-rate and varied from 5.5 GPa at $10^{-4}\,s^{-1}$ to 8.3 GPa at $10^3\,s^{-1}$. For low strain rates and uniaxial stresses deformation occurs mainly by dislocation movement. The dislocations may align themselves to form shear microbands, but for uniaxial strain basal twins are also observed. Cracks initiate at dislocation pile-ups at grain boundaries [55] or due to the interaction of twins or slip planes with grain boundaries [56]. The dislocation bands and twins observed in the ablation angular particles and the fact that they are crystalline with the same allotropic forms of the original material confirms that these particles are formed by deformation and fracture. Experiments carried out in sapphire single crystals under shock-loading conditions with strain rates similar to those found in femtosecond laser processing, showed that basal twinning is the predominant deformation mechanism in these conditions [57]. Molecular dynamics simulations of α-alumina under hypervelocity impact carried out by Zhang [58] revealed that when a reinforced projectile impacts an alumina single crystal at high velocity it induces a shock wave that propagates through the substrate. Behind the elastic wave front, a region with an amorphous structure forms around the impact zone, due to the high temperature and pressure generated by the impact loading. On the other hand, the local temperature of the substrate around the impact point rises above the boiling and sublimation points. As a consequence, the impacted region melts and vaporizes and liquid droplets are ejected. Ahead of the molten region the loading results in the formation of abundant twins, which effectively relieve the shear stresses, leaving the outside substrate material perfectly crystalline except for a few pyramidal and basal slips/twins. When the elastic wave front reaches the bottom free surface and returns as a rarefaction wave, it relieves pressure and shear stresses in the substrate and cracks form around damaged regions left by previous deformations, spallation and ejection of material within an hourglass-shaped volume occurs. This description is consistent with the shape and evolution of the craters depicted in Fig. 1 and with the ablation debris observed in Figs. 8 and 9. This similarity clearly demonstrates the role of thermomechanical effects in the ultrafast laser ablation of single crystalline sapphire.

5. Conclusions

When wafers of single-crystal sapphire cut parallel to the (0 1 2) planes are treated with a 500 fs, 1030 nm wavelength laser radiation using intensities slightly larger than the ablation threshold self-ordered periodic structures with an average spatial periodicity of ~300 nm are observed. For higher fluences the interaction is more disruptive and extensive fracture, exfoliation, and projection

of ablation debris occurs. The ablation process results in the formation of spherical nanoparticles about 50 nm in diameter, with an amorphous structure, directly emitted by the material during ablation, composite amorphous particles between 150 and 400 nm in size formed by coalescence of the precedent particles during the cooling down of the ablation plume, rounded resolidified particles about 100–500 nm in size, and angular particles with a lamellar structure and a large density of deformation twins. The last two types of particles are crystalline, with α-alumina crystal structure. These particles are ejected as a result of the ablation process, as liquid droplets and by mechanical exfoliation, respectively. The observed ablation behavior is similar to the phenomena occurring in crystalline α-alumina during high-energy micro-impacts, clearly demonstrating the role of thermomechanical effects in the ablation of single crystalline sapphire.

Acknowledgements

This work was carried out with the financial support from Fundação para a Ciência e a Tecnologia, project PTDC/FIS/102127/2008. One of the authors, S.P. Sharma, gratefully acknowledges Instituto Superior Técnico and Fundação para a Ciência e a Tecnologia (FCT) for the postdoctoral fellowship provided through project PTDC/FIS/102127/2008 and SFRH/BPD/78871/2011.

References

[1] P. Balling, J. Schou, Femtosecond-laser ablation dynamics of dielectrics: basics and applications for thin films, Rep. Prog. Phys. 76 (2013) 036502.
[2] L. Jiang, H.L. Tsai, Energy transport and material removal in wide bandgap materials by a femtosecond laser pulse, Int. J. Heat Mass Transfer 48 (2005) 487–499.
[3] E.G. Gamaly, A.V. Rode, B. Luther-Davies, V.T. Tikhonchuk, Ablation of solids by femtosecond lasers: ablation mechanism and ablation thresholds for metals and dielectrics, Phys. Plasmas 9 (2002) 949–957.
[4] E.G. Gamaly, The physics of ultra-short laser interaction with solids at non-relativistic intensities, Phys. Rep. 508 (2011) 91–243.
[5] P.E. Dyer, S.D. Jenkins, J. Sidhu, Development and origin of conical structures on XeCl laser ablated polymide, Appl. Phys. Lett. 49 (1986) 453–455.
[6] V. Oliveira, F. Simões, R. Vilar, Column growth mechanics during KrF laser micromaching of Al_2O_3-TiC ceramics, Appl. Phys. A 81 (2005) 1157–1162.
[7] V. Oliveira, R. Vilar, Characterization of columns grown during KrF laser micromachining of Al_2O_3-TiC ceramics, J. Mater. Sci. 18 (2003) 1123–1130.
[8] F. Sanchez, J.L. Morenza, R. Aguiar, J.C. Delgado, M. Varela, Dynamics of the hydrodynamical growth of columns on silicon exposed to excimer-laser irradiation, Appl. Phys. A 66 (1998) 83–86.
[9] V. Oliveira, M. Sivakumar, R. Vilar, A mathematical description of surface texture development in laser-ablated dentin, J. Appl. Phys. 100 (2006) 104701.
[10] O. Conde, A. Kar, J. Mazumder, Laser chemical vapor deposition of TiN dots: a comparison of theoretical and experimental results, J. Appl. Phys. 72 (1992) 754.
[11] J. Wang, C. Guo, Numerical study of ultrafast dynamics of femtosecond laser-induced surface structure formation on noble metals, J. Appl. Phys. 102 (2007).
[12] J. Bonse, J. Kruger, S. Hohm, A. Rosenfeld, Femtosecond laser-induced periodic surface structures, J. Laser Appl. 24 (2012) 042006.
[13] F. Keilmann, Y.H. Bai, Periodic surface structures frozen into CO_2 laser-melted quartz, Appl. Phys. A 29 (1982) 9–18.
[14] J.E. Sipe, J.F. Young, J.S. Preston, H.M.V. Driel, Laser-induced periodic surface structure. I. Theory, Phys. Rev. B 27 (1983) 1141–1154.
[15] J. Bonse, A. Rosenfeld, J. Krüger, On the role of surface plasmon polaritons in the formation of laser-induced periodic surface structures upon irradiation of silicon by femtosecond laser pulses, J. Appl. Phys. 106 (2009) 104910.
[16] A. Cunha, A.P. Serro, V. Oliveira, A. Almeida, R. Vilar, M.-C. Durrieu, Wetting behaviour of femtosecond laser textured Ti–6Al–4V surfaces, Appl. Surf. Sci. 265 (2013) 688–696.
[17] V. Zorba, E. Stratakis, M. Barberoglou, E. Spanakis, P. Tzanetakis, S.H. Anastasiadis, C. Fotakis, Biomimetic artificial surfaces quantitatively reproduce the water repellency of a lotus leaf, Adv. Mater. 20 (2008) 4049.
[18] V. Oliveira, B. Nunes, R. Vilar, Wetting response of KrF laser ablated polyimide surfaces, Nucl. Instrum. Methods B 268 (2010) 1626–1630.
[19] T. Baldacchini, J.E. Carey, M. Zhou, E. Mazur, Superhydrophobic surfaces prepared by microstructuring of silicon using a femtosecond laser, Langmuir 22 (2006) 4917–4919.
[20] C. Liang, H. Wang, J. Yang, Y. Yang, X. Yang, Surface modification of cp-Ti using femtosecond laser micromachining and the deposition of Ca/P layer, Mater. Lett. 62 (2008) 3783–3786.
[21] A. Cunha, V. Oliveira, A.P. Serro, O.F. Zouani, A. Almeida, M.-C. Durrieu, R. Vilar, Ultrafast laser texturing of Ti–6Al–4V surfaces for biomedical applications ICALEO 2013, LIA Pub. 616, vol. 106, Laser Institute of America, Orlando, FL, USA, 2013, pp. 910–918.
[22] V.V. Iyengar, B.K. Nayak, M.C. Gupta, Optical properties of silicon light trapping structures for photovoltaics, Sol. Energy Mat. Sol. Cells 94 (2010) 2251–2257.
[23] Y. Shimotsuma, P.G. Kazansky, J. Qiu, K. Hirao, Self-organized nanogratings in glass irradiated by ultrashort light pulses, Phys. Rev. Lett. 91 (2003) 247405.
[24] V.R. Bhardwaj, E. Simova, P.P. Rajeev, C. Hnatovsky, R.S. Taylor, D.M. Rayner, P.B. Corkum, Optically produced arrays of planar nanostructures inside fused silica, Phys. Rev. Lett. 96 (2006) 057401–057404.
[25] D. Wortmann, J. Gottmann, N. Brandt, H. Horn-Solle, Micro- and nanostructures inside sapphire by fs-laser irradiation and selective etching, Opt. Express 16 (2008) 1517–1522.
[26] J. Bai, G. Cheng, X. Long, Y. Wang, W. Zhao, G. Chen, R. Stoian, R. Hui, Polarization behavior of femtosecond laser written optical waveguides in Ti:Sapphire, Opt. Express 20 (2012) 15053.
[27] P.P. Rajeev, M. Gertsvolf, C. Hnatovsky, E. Simova, R.S. Taylor, P.B. Corkum, D.M. Rayner, V.R. Bhardwaj, Transient nanoplasmonics inside dielectrics, J. Phys. B: At. Mol. Opt. Phys. 40 (2007) S273–S282.
[28] E.N. Glezer, E. Mazur, Ultrafast-laser driven micro-explosions in transparent materials, Appl. Phys. Lett. 71 (1997) 882–884.
[29] E.G. Gamaly, S. Juodkazis, K. Nishimura, H. Misawa, B. Luther-Davies, L. Hallo, P. Nicolai, V.T. Tikhonchuk, Laser-matter interaction in the bulk of a transparent solid: confined microexplosion and void formation, Phys. Rev. B 73 (2006) 214101.
[30] S. Juodkazis, H. Misawa, I. Maksimov, Thermal accumulation effect in three-dimensional recording by picosecond pulses, Appl. Phys. Lett. 85 (2004) 5239–5241.
[31] S. Juodkazis, K. Nishimura, H. Misawa, In-bulk and surface structuring of sapphire by femtosecond pulses, Appl. Surf. Sci. 253 (2007) 6539–6544.
[32] S. Juodkazis, K. Nishimura, H. Misawa, T. Ebisui, R. Waki, S. Matsuo, T. Okada, Control over the crystalline state of sapphire, Adv. Mater. 18 (2006) 1361–1364.
[33] S. Juodkazis, K. Nishimura, S. Tanaka, H. Misawa, E.G. Gamaly, B. Luther-Davies, L. Hallo, P. Nicolai, V.T. Tikhonchuk, Laser-induced microexplosion confined in the bulk of a sapphire crystal: evidence of multimegabar pressures, Phys. Rev. Lett. 96 (2006) 166101.
[34] V. Mizeikis, S. Kimura, N.V. Surovtsev, V. Jarutis, A. Saito, H. Misawa, S. Juodkazis, Formation of amorphous sapphire by a femtosecond laser pulse induced microexplosion, Appl. Surf. Sci. 255 (2009) 9745–9749.
[35] V.N. Kurlov, Sapphire: properties, growth, and applications, in: K.H.J. Buschow, R.W. Cahn, M.C. Flemings, B. Ilschner, E.J. Kramer, S. Mahajan, P. Veyssière (Eds.), Encyclopedia of Materials: Science and Technology, Pergamon, Amsterdam, 2001, pp. 8259–8264.
[36] W. Rasband, ImageJ-Image Processing and Analysis in Java, National Institutes of Health, Research Services Branch, National Institute of Mental Health, Bethesda, Maryland, USA, 2013.
[37] J.M. Liu, Simple technique for measurements of pulsed Gaussian-beam spot sizes, Opt. Lett. 7 (1982) 196–198.
[38] M. Kadleikova, J. Breza, M. Vesely, Raman spectra of synthetic sapphire, Microelectron. J. 32 (2001) 955–958.
[39] F. Watanabe, D.G. Cahill, B. Gundrum, R.S. Averback, Ablation of crystalline oxides by infrared femtosecond laser pulses, J. Appl. Phys. 100 (2006) 083519.
[40] M. Henyk, R. Mitzner, D. Wolffframm, J. Reif, Laser-induced ion emission from dielectrics, Appl. Surf. Sci. 154–155 (2000) 249–255.
[41] X. Li, T. Jia, D. Feng, Z. Xu, Ablation induced by femtosecond laser in sapphire, Appl. Surf. Sci. 225 (2004) 339–346.
[42] M.N. Christensen, J. Byskov-Nielsen, B.H. Christensen, P. Balling, Single-shot ablation of sapphire by ultrashort laser pulses, Appl. Phys. A 101 (2010) 279–282.
[43] O. Uteza, B. Bussière, F. Canova, J.-P. Chambaret, P. Delaporte, T. Itina, M. Sentis, Laser-induced damage threshold of sapphire in nanosecond, picosecond and femtosecond regimes, Appl. Surf. Sci. 254 (2007) 799–803.
[44] D. Kim, W. Jang, T. Kim, A. Moon, K. Lim, M. Lee, I. Sohn, S. Jeong, Nanostructure and microripple formation on the surface of sapphire with femtosecond laser pulses, J. Appl. Phys. 111 (2012) 093518.
[45] D. Sherman, I. Be'ery, Fracture mechanisms of sapphire under bending, J. Mater. Sci. 35 (2000) 1283–1293.
[46] T. Vodenitcharova, L.C. Zhang, I. Zarudi, Y. Yin, H. Domyo, T. Ho, M. Sato, The effect of anisotropy on the deformation and fracture of sapphire wafers subjected to thermal shocks, J. Mater. Process. Technol. 194 (2007) 52–62.
[47] M. Lancry, B.P. Cook, J. Canning, Nanogratings and molecular oxygen formation during femtosecond laser irradiation in silica, in: M. Lancry, B.P. Cook, J. Canning (Eds.), IQEC/CLEO Pacific Rim 2011, Australian Optical Society (AOS), Sydney, Australia, 2011, pp. 208–210.
[48] N.G. Semaltianos, Nanoparticles by laser ablation, Crit. Rev. Solid State Mater. Sci. 35 (2010) 105–124.
[49] D. Perez, L.J. Lewis, Ablation of solids under femtosecond laser pulses, Phys. Rev. Lett. 89 (2002) 255504.
[50] W.T. Ashurst, B.L. Holian, Droplet formation by rapid expansion of a liquid, Phys. Rev. E 59 (1999) 6742–6752.
[51] S. Noel, J. Hermann, T. Itina, Investigation of nanoparticle generation during femtosecond laser ablation of metals, Appl. Surf. Sci. 253 (2007) 6310–6315.

[52] T.E. Itina, K. Gouriet, L.V. Zhigilei, S. Noel, J. Hermann, M. Sentis, Mechanisms of small clusters production by short and ultra-short laser ablation, Appl. Surf. Sci. 253 (2007) 7656–7661.
[53] H.K. Park, J.R.F. Haglund, Laser ablation and desorption from calcite from ultraviolet to mid-infrared wavelengths, Appl. Phys. A 64 (1997) 431–438.
[54] H.M. Chan, B.R. Lawn, Indentation deformation and fracture of sapphire, J. Am. Ceram. Soc. 71 (1988) 29–35.
[55] J.M. Staehler, W.W. Predebon, B.J. Pletka, G. Subhasha, Micromechanisms of deformation in high-purity hot-pressed alumina, Mater. Sci. Eng. A 291 (2000) 37–45.
[56] J. Lankford, W.W. Predebon, J.M. Staehler, G. Subhash, B.J. Pletka, C.E. Anderson, The role of plasticity as a limiting factor in the compressive failure of high strength ceramics, Mech. Mater. 29 (1998) 205–218.
[57] Y. Wang, D.E. Mikkola, {0 0 0 1} <1 0 1 0> Slip and basal twinning in sapphire single crystals shock-loaded at room temperature, J. Am Ceram. Soc. 72 (1992) 3252–3256.
[58] C. Zhang, R.K. Kalia, A. Nakano, P. Vashishta, P.S. Branicio, Deformation mechanisms and damage in α-alumina under hypervelocity impact loading, J. Appl. Phys. 103 (2008) 083508.